Vortex Shedding from a Circular Cylinder in shear-thinning Carreau Fluids

Shantanu Bailoor, Jung-Hee Seo, and Rajat Mittal
Physics of Fluids **31**, 011703 (2019); https://doi.org/10.1063/1.5086032

Mechanical Engineering, The Johns Hopkins University, Baltimore, MD 21218, USA

Results from numerical simulations of two-dimensional, shear-thinning Carreau fluid flow over an unconfined circular cylinder are presented in this paper. Parametric sweeps are performed over the various Carreau model parameters and trends of the time-averaged force coefficients and vortex characteristics are reported. In general, increased shear-thinning results in lower viscous forces on the body but greater pressure forces, resulting in a complex non-monotonic drag response. Lift forces generally increased with shear-thinning due to the dominant pressure contribution. The decrease in fluid viscosity also led to shorter vortex formation lengths and the consequent rise in Strouhal frequency of vortex shedding. It is expected that these results will be useful for verification of computational models of unsteady non-Newtonian flows.

Non-Newtonian fluids are routinely encountered in the form of industrial fluids (e.g. polymer solutions, emulsions, molasses, silicone oils) in several arenas such as the food, paper, process engineering [1] and bio-chemical industries. Many common biological fluids like honey, blood, synovial fluid, saliva, and semen also belong to this class of fluids. Non-Newtonian fluids are characterized by complex constitutive properties, such as shear-dependent viscosity, fluid elasticity and the dependence of fluid properties on deformation history. Fluids like blood can be characterized as viscous inelastic and are classified as shear-thinning or shear-thickening based on the influence of deformation on fluid viscosity. A simple inelastic viscous fluid may be represented as a Generalized Newtonian fluid, in which shear-stress has linear proportionality with shear-rate, but the coefficient of proportionality has a non-linear dependence on shear-rate. Generalized Newtonian fluids are commonly modeled using the power-law or the Carreau-Yasuda models [2,3].

A large body of work involving simulations of flow of power-law fluids over bluff bodies exists. For instance, Bell and Surana [4] performed finite-element simulations of power-law flow through 2D ducts, inside square, driven cavities and in sudden expansions. Chhabra and colleagues have analyzed steady power-law flow over unconfined [5] and confined [6] circular cylinders. Additionally, stability analysis was performed for the wake of the unconfined cylinder [7]. The group also modeled unsteady flow over unconfined circular cylinder [8] and heat-transfer in steady flow [9]. Finally, data is also available for power-law flow past elliptic [10], square [11] and triangular [12] cylinders.

Although a significant corpus of numerical simulations exists for power-law fluids, the model is not suitable for applications where distinct upper and lower bounds, with smooth transitions, need to be defined for fluid viscosity. Thus, other models like the Casson, Cross and the Carreau-Yasuda models and their variants have recently received attention for a variety of applications including, but not limited to, hemodynamic modeling [13,14,15,16], convection in porous media [17] and magnetohydrodynamic flows [18]. Despite its increasing popularity, very little canonical simulation data is available in literature for Carreau fluids. Coelho and Pinho [19,20,21] performed experiments of weak polymer solution flow over circular cylinders, and fitted Carreau-Yasuda model parameters for the fluid viscosity response. It is however acknowledged by the authors that the polymer solutions are viscoelastic, and thus application of the Carreau-Yasuda model to these fluids is somewhat suspect. Haque et al. [22] studied the effect of shear-thinning and shear-thickening Carreau fluids on the transition of flow in a square shear-driven cavity from two- to three-dimensional. Lashgari et al. [23] used linear stability theory and direct numerical simulation to determine the critical Reynolds number at which the wake of a circular cylinder immersed in Carreau fluid becomes unstable. Recently, Pantokratoras [24] simulated steady Carreau flow over a circular cylinder and reported trends of drag coefficient variation with changes in model parameters. To the best of our knowledge, computational work on Carreau fluid flow past circular cylinders has been limited to steady flows and no work exists which reports data on unsteady flow characteristics involving bluff bodies. Such data would be particularly useful for benchmarking codes that employ this model. To this end, the present study reports quantitative data for Carreau flow past a circular cylinder. Simulations are conducted for a range of Carreau fluid parameters and forces, pressures, vortex shedding frequencies and wake parameters are presented.

In this report, we present results from a set of simulations of Carreau fluid flow with velocity U_∞ over an unconfined cylinder of diameter D. All simulations were performed using a finite-difference-based, incompressible fluid-structure interaction solver, which uses the sharp-interface immersed boundary method of Mittal et al. [25]. The method uses a second-order accurate ghost-cell formulation for imposing boundary conditions over Cartesian grids and second-order spatial and temporal discretization. The original solver integrates the incompressible Navier-Stokes equations in the conservative form (Equations (1) & (2)) using a fractional step method.

$$\nabla \cdot \boldsymbol{u} = 0 \tag{1}$$

$$\frac{\partial \boldsymbol{u}}{\partial t} + \nabla \cdot (\boldsymbol{uu}) = -\nabla p + \nabla \cdot (2\mu \boldsymbol{S}) \tag{2}$$

In the above equations, all symbols have their usual meaning. The fractional step method consists of an advection-diffusion (AD) step, followed by velocity correction, which enforces the divergence-free constraint via the solution of the pressure Poisson equation. In the above equations, $\boldsymbol{S}$ is the symmetric strain-rate tensor, relates to the velocity gradient tensor as $\boldsymbol{S} = \frac{1}{2}(\nabla \boldsymbol{u} + \nabla \boldsymbol{u}^T)$ and μ is the non-dimensional kinematic viscosity, which for Newtonian fluids is a constant. This solver has been modified to solve Carreau fluids by simply replacing the Newtonian viscosity by an expression governing a Carreau fluid:

$$\mu = \mu_\infty + (\mu_0 - \mu_\infty)[1 + (\lambda\dot{\gamma})^2]^{\left(\frac{n-1}{2}\right)} \tag{3}$$

In equation (3), viscosity at shear-rate $\dot{\gamma}$ is interpolated between limiting values at zero (μ_0) and infinite shear (μ_∞) and λ determines the shear-rate at which viscosity transitions (as $\sim\dot{\gamma}^{n-1}$) from the zero-shear viscosity plateau to power-law-like behavior. For shear-thinning fluids, $n < 1$. In this report, we perform parametric sweeps over n, λ and μ_∞, and report values for the Strouhal number of vortex shedding, and the time-averaged drag and the RMS lift coefficients. The viscous ($\boldsymbol{F}_v$) and pressure ($\boldsymbol{F}_P$) forces on the body, per unit depth, are calculated as described in equation (4):

$$\boldsymbol{F}_V = \oint \mu(\nabla \boldsymbol{u} + \nabla \boldsymbol{u}^T) \cdot \boldsymbol{n} ds, \qquad \boldsymbol{F}_P = \oint p\boldsymbol{n} ds \tag{4}$$

The streamwise and cross-stream components of the above forces constitute the drag and lift experienced by the body, respectively. In this report, the normalized drag and lift forces are expressed via the respective force coefficients, C_D and C_L, defined in equation (5):

$$C_D = \frac{\oint [\mu(\nabla \boldsymbol{u} + \nabla \boldsymbol{u}^T) \cdot \boldsymbol{n} + p\boldsymbol{n}]_x ds,}{\frac{1}{2}\rho U_\infty^2 D} \qquad C_L = \frac{\oint [\mu(\nabla \boldsymbol{u} + \nabla \boldsymbol{u}^T) \cdot \boldsymbol{n} + p\boldsymbol{n}]_y ds,}{\frac{1}{2}\rho U_\infty^2 D} \tag{5}$$

For the sake of brevity, trends of pressure and viscous components of force coefficients are not described herein.

To verify the ability of the present solver to accurately predict critical flow phenomena and other derived quantities, we simulated the several cases presented by Lashgari et al. [23]. In the first set of results, we simulated flow of shear-thinning Carreau fluid over an unconfined circular cylinder at a subcritical Reynolds number 10

($Re = U_\infty D/\mu_0$). Setting $\mu_\infty = 0.001\mu_0$ and $\lambda = 10$, the power-law index was varied between 0.4 and 1.0. The observed steady-state drag coefficients are reported in Table 1, showing agreement to within 5% of published results [23, 24]. Additionally, through numerical simulations, we verified the neutral stability curve for the steady cylinder wake, as reported by Lashgari et al. [23]. To do this, we simulated the fate of the cylinder wake at ±5% of the reported critical Reynolds number for each power-law index with $\mu_\infty = 0.001\mu_0$ and $\lambda = 10$. It is expected the subcritical and supercritical simulations respectively result in steady and unsteady wakes. Since the Reynolds numbers are very close to the corresponding critical values, the simulations need to be run for a long time ($tU_\infty/D \sim 900$) before wake instabilities may observed. The wake fates are also tabulated in Table 1 which indicate that with increasing shear-thinning tendency of the fluid, the critical Reynolds number for the wake instability decreases. This is consistent with the findings of Coelho and Pinho [19,20,21]. It further shows an excellent corroboration of the critical Reynolds number, obtained using linear stability theory by Lashgari et al. [23]. Particularly, the case of $n = 0.4$ indicates that the solver can predict changes in flow regimes for very small changes in flow Reynolds numbers. This demonstrates the ability of the present solver to accurately predict fundamental flow phenomena, in addition to the forces experienced by the body.

n	Drag coefficient for subcritical Re 10.					Wake stability analysis				
	C_D (Present)	C_D [23]	% Error	C_D [24]	% Error	Critical Re [23]	Subcritical test		Supercritical test	
							Re	Wake fate	Re	Wake fate
0.4	1.19	1.24	4.03	1.22	2.45	20	19	Steady	21	Unsteady
0.6	1.67	1.71	2.34	1.67	0.00	31	29	Steady	33	Unsteady
0.8	2.23	2.25	0.89	2.20	1.36	47	45	Steady	49	Unsteady
1.0	2.89	2.81	2.85	2.75	5.05	77	74	Steady	80	Unsteady

Table 1: Results for steady-state drag coefficient at subcritical *Re* 10 and cylinder wake stability analysis for various values of power-law index *n*. In each set of simulations, $\mu_\infty = 0.001\mu_0$ and $\lambda = 10.0$. Comparison with relevant published data [23,24] is provided indicating very good agreement in each case.

For all unsteady results presented herein, the cylinder is placed in a $40D\times40D$ domain, centered at ($15D,20D$), and discretized using a (401×385) non-uniform Cartesian grid. A rectangular region of size $4D\times4D$ extending into the wake is provided with high, isotropic resolution ($\Delta x=\Delta y=D/50$). Beyond this region the grid is stretched in all directions. Downstream of the cylinder the change in size of consecutive cells constrained to < 3% to prevent excessive numerical dissipation of solution. This grid resolution was selected after testing the effect of grid refinement on extracted quantities like the drag and lift coefficients and their pressure and viscous components. It was observed that halving the grid spacing resulted in a maximum deviation in the derived quantities of < 1%. The simulation Reynolds number is defined with respect to the reference zero-shear viscosity ($Re_0 = U_\infty D/\mu_0$), the fluid relaxation time λ is defined in terms of the Carreau number ($Cu = U_\infty \lambda/D$), and μ_∞ is defined relative to μ_0 via the non-dimensional parameter $k_\mu = \mu_\infty/\mu_0$. The baseline values for the model parameters are: $Re_0 = 100$, $k_\mu = 0.5$, $n = 0.5$ and $Cu = 1.0$. This choice of parameters is based on the desire to keep the maximum local Reynolds number ($U_\infty D/\mu$) in the range where the cylinder wake does not develop spanwise instabilities and the flow remains two-dimensional (< 200). All simulations result in the eventual development of periodic vortex shedding and averages are accumulated over at least 80 shedding cycles to ensure statistical convergence.

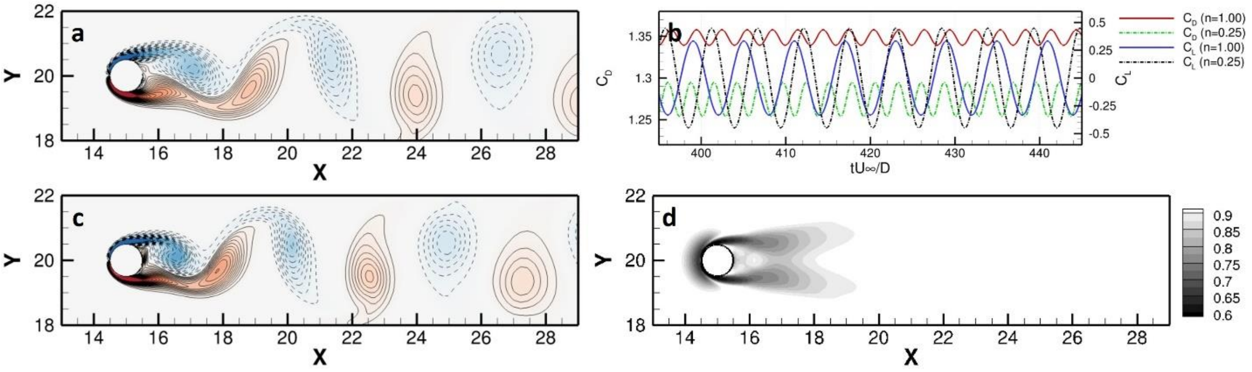

FIG 1: (a), (c) Vorticity contours at $tU_\infty/D = 800$ using $n = 1.0$ and $n = 0.25$, respectively. Solid and dashed lines are used to denote positive and negative vorticity, respectively. (b) Time varying drag and lift coefficients for the two simulation cases and (d) time-averaged normalized viscosity contour plot for $n = 0.25$.

In the first parameter sweep n is varied from 1.00, the Newtonian limit, to 0.25 in increments of 0.25. As n is decreased, the fluid thins more rapidly with shear. FIG 1 (a) and (c) illustrate vorticity contours in the cylinder wake, using $n = 1.0$ (Newtonian) and $n = 0.25$ (Shear-thinning), respectively at $tU_\infty/D = 800$. The two snapshots are taken at very similar phases during the vortex shedding cycle and it is observed that the attached wake and shed vortices in the shear-thinning case are smaller than those in the Newtonian case. The time-varying drag and lift coefficients in each case, during the periodic vortex shedding phase are illustrated in FIG 1 (b). It is observed shear-thinning resulted in a decrease in the average drag, but increase in the fluctuating components of both, drag and lift coefficients. Finally, FIG 1 (d) shows the time-averaged normalized viscosity contour (μ/μ_0) for the $n = 0.25$ case. Regions of low viscosity are concentrated around the stagnation point, the attached boundary layer and the near-wake. On the other hand, viscosity appears to be constant in the relatively low-shear regions of the far-wake and free-stream.

FIG 2 (a) shows the variation of time-averaged drag and RMS lift coefficients with shear-thinning index, *n*. It also presents corresponding values reported by Liu et al. [27] for Newtonian flow at Reynolds number 100, with agreement to within 3% of those obtained for $n = 1.0$. As the fluid becomes increasingly shear-thinning, the average drag coefficient decreases monotonically, while the fluctuations in drag increase, leading to a general reduction in total drag (FIG 1 (b)). The decrease in average drag is attributed almost entirely to a drop in the mean viscous forces on the body (which reduces from 0.339 to 0.256), while the mean pressure forces do not show significant changes (increased from 1.010 to 1.020). The increase in the fluctuating component of drag and lift coefficients is related to smaller vortex formation lengths associated with increasingly shear-thinning fluids. FIG 2 (b) shows trends of Strouhal number ($St = fD/U_\infty$) and vortex formation length variations with *n*, and a comparison with published results for *St* from Roshko [28] and Williamson [29]. Defined by Williamson [29], the vortex formation length is the distance downstream from the cylinder axis to a point where the magnitude of the velocity fluctuations is maximized on the wake center line. In addition to increasing the fluctuating components, a shorter formation length also results in an increase in the vortex shedding frequency, which is observed in the sweep along *n*; as *n* is decreased, the Strouhal number increases monotonically. The Strouhal number at the Newtonian limit was observed to be 0.167, which agrees very well with experimental results of Williamson [29] ($St = 0.165$) and Roshko [28] ($St = 0.167$).

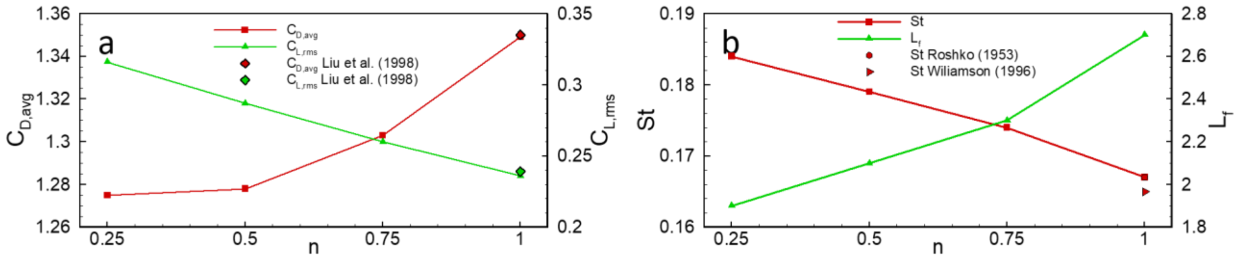

FIG 2: Variation of (a) time-averaged drag, RMS lift and (b) Strouhal number and vortex formation length with power-law index, *n*. For comparison, time-averaged drag and RMS lift coefficients from Newtonian simulations (n = 1.00) of and Liu et al. [27] and Strouhal number measurements by Roshko [28], and Williamson [29] are provided. In (a) red symbols indicate drag coefficient values and green symbols denote RMS lift coefficient values, while in (b) red symbols are used for Strouhal number measurements from literature.

Next, we vary the Carreau number, *Cu*, keeping all other variables at their baseline values. This parameter determines the shear-rate at which viscosity transitions from the zero-shear plateau to the power-law region; larger values of *Cu* result in transition occurring at lower shear-rates and vice-versa. The tested values of *Cu* are 0.01, 0.10, 1.00 and 10.0. FIG 3 (a) and (b) show contour plots of instantaneous vorticity at $tU_\infty/D = 800$ and time-averaged normalized viscosity for $Cu = 10.0$, respectively. As observed in the sweep over *n*, shear-thinning induced by changing *Cu* also resulted in early vortex separation from the boundary layer. The normalized viscosity field (FIG 3 (b)), on the other hand, shows a different trend, when compared with the corresponding plot for $n = 0.25$. Regions of low viscosity are observed to extend beyond the cylinder boundary layer, nearly twice as far upstream and even into the far wake. A large Cu shifts the point of transition from the zero-shear plateau, in the rheological chart for a Carreau fluid, to the left. This increases the sensitivity of fluid viscosity to changes in local shear-rate, resulting in more regions of the flow exhibiting shear-thinning behavior. Similar viscosity distribution was also observed by Lashgari et al. [23], albeit for subcritical flows.

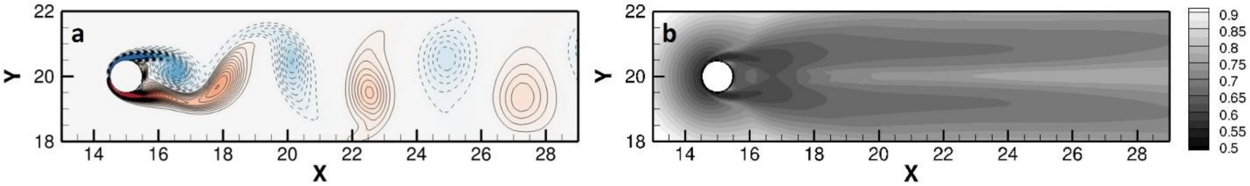

FIG 3: Contour plots of (a) vorticity and (b) time-averaged normalized viscosity for $Cu = 10.0$.

As Cu is increased from 0.01 to 1.00, the time-average drag coefficient decreases (FIG 4 (a)), due to lower friction drag on the cylinder, with relatively small changes in the surrounding pressure field. However, from $Cu = 1.00$ to $Cu = 10.0$, the average total drag increases, even though the viscous drag continues to diminish in magnitude. This increase is due to a significant rise in pressure forces, resulting from an increase in base suction. The RMS lift coefficient (FIG 4 (a)), on the other hand, first exhibits about a 2% drop with increase in Cu from 0.01 to 0.10, then increases for the remainder of the range of tested Cu. The inverse trend is observed with the formation length (FIG 4 (b)), which shows a marginal increase from $Cu = 0.01$ to 0.1, then a monotonic decrease up to $Cu = 10.0$. FIG 4 (b) shows a monotonic increase in Strouhal number with Cu.

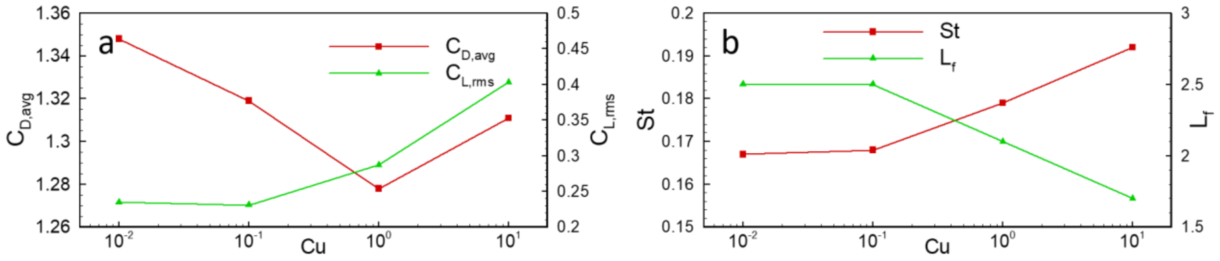

FIG 4: Variation of (a) time-averaged drag, RMS lift coefficients and (b) Strouhal number and vortex formation length versus Cu.

Finally, the viscosity ratio k_μ is varied while keeping other parameters at their baseline values. Beginning with the Newtonian case with $k_\mu = 1.0$, the viscosity ratio is decreased up to $k_\mu = 0.10$. Reducing k_μ decreases the lower-limit on viscosity, increasing the maximum local Reynolds number in the simulation. While it is acknowledged that $k_\mu = 0.10$ could potentially lead to local Reynolds numbers beyond the range where the cylinder wake remains two-dimensional, this range is chosen to demonstrate an appreciable variation in measured quantities and sampling sufficiently many values of k_μ to illustrate a trend. The resulting vortex street (FIG 5 (a)), unsurprisingly, shows smaller vortices and earlier separation, compared to the Newtonian case. The time-averaged normalized viscosity contour (FIG 5 (b)) shows similar concentration of low-viscosity regions as the n = 0.25 case, with a lower minimum viscosity of about 0.24.

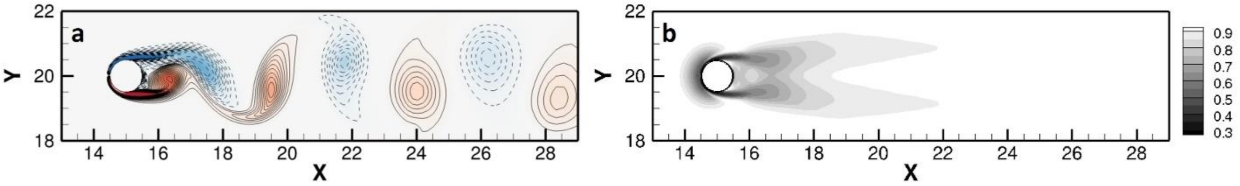

FIG 5: Contour plots of (a) vorticity and (b) time-averaged normalized viscosity for k_μ = 0.10.

The effect of k_μ on time-averaged drag and lift coefficients, Strouhal number and vortex formation length is illustrated in FIG 6 (a) and (b). The mean drag coefficient decreases with k_μ, which is explained by a reduction in friction drag and relatively small changes in the pressure drag. The shorter formation lengths also lead to an increase in the fluctuating component of the forces, resulting in larger RMS lift with decreasing k_μ, and increase in the Strouhal frequency (FIG 6 (b)).

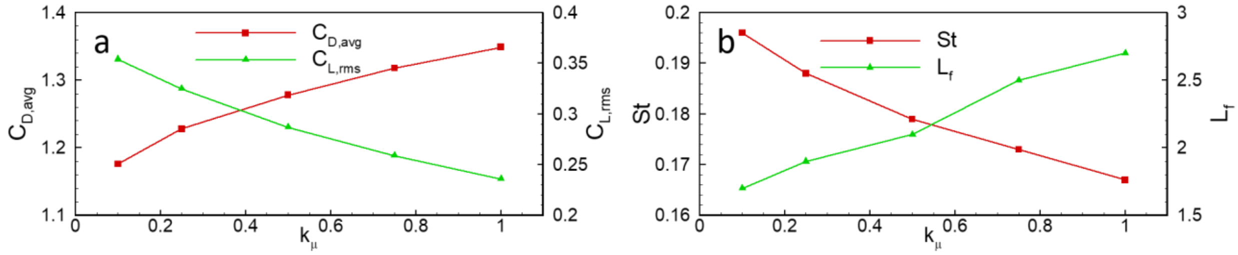

FIG 6: Trends of (a) time-averaged drag, RMS lift coefficients and (b) Strouhal number and formation length with k_μ.

In summary, laminar vortex-shedding from an unconfined circular cylinder in shear-thinning Carreau fluids is simulated. The effect of varying model parameters on the cylinder wake and the force experienced by it is quantified. While the cylinder wake for the tested Carreau parameters resembles that from a Newtonian fluid, and vortex shedding remains periodic, the forces experienced by the cylinder show significant sensitivity to model parameters. Shear-thinning results in a decrease in the shear forces on the cylinder, but an increase in the base suction which can result in a complex, non-monotonic relation between fluid shear-thinning tendency and the time-averaged drag. On the other hand, the shear contribution to lift on the body is marginal, due to which, the RMS lift experienced by the body generally increases with shear-thinning tendency. In the steady flow regime, shear-thinning results in an increase in the recirculation bubble size [23], due to a decrease in shear-stress in the high shear regions adjacent to the recirculation bubble. On the contrary, in the unsteady regime, the increase in base suction due to shear-thinning drives the low-pressure vortices closer to the cylinder. This leads to a shorter and narrower formation region, resulting in a smaller attached vortex and formation length. Scaling inversely with the formation length, the Strouhal frequency of vortex shedding increases with shear-thinning. The spatial distribution of viscosity appears to be more sensitive to changes in the Carreau number as compared to the power-law index or the viscosity ratio. The results obtained in this study can serve as benchmark for verification of Carreau flow solvers.

Acknowledgement

This work was sponsored by the National Science Foundation (NSF) Grant CBET 1511200.

References

1. Chhabra RP and Richardson JF (1999) Non-Newtonian Flow in Process Industries: Fundamentals and Engineering Applications; Butterworth-Heinemann, Oxford, UK, ISBN: 0-7506-3770-6.

2. Carreau PJ (1972) Rheological Equations from Molecular Network Theories. J. Rheol, 16(1):99-127

3. Yasuda K (1979) Investigation of the analogies between viscometric and linear viscoelastic properties of polystyrene fluids, PhD Thesis, Massachusetts Institute of Technology.

4. Bell BC and Surana KS (1994) p-Version Least Squares Finite Element Formulation for Two-Dimensional Incompressible, Non-Newtonian Isothermal and non-Isothermal Fluid Flow. Int. J. Numer. Meth. Fluids, 18: 127-162.

5. Bharti RP, Chhabra RP and Eswaran V (2006) Steady Flow of Power Law Fluids across a Circular Cylinder. Can. J. Chem. Eng., 84: 406-421.

6. Bharti RP, Chhabra RP and Eswaran V (2007) Two-Dimensional Steady Poiseuille Flow of Power-Law Fluids Across a Circular Cylinder in a Plane Confined Channel: Wall Effects and Drag Coefficients. Ind. Eng. Chem. Res, 46: 3820-3840.

7. Sivakumar P, Bharti RP and Chhabra RP (2006) Effect of power-law index on critical parameters for power-law flow across an unconfined circular cylinder. Chem. Eng. Sci., 61:6035-6046.

8. Patnana VK, Bharti RP and Chhabra RP (2009) Two-dimensional unsteady flow of power-law fluids over a cylinder. Chem. Eng. Sci., 64:2978-2999.

9. Bharti RP, Chhabra RP and Eswaran V (2007) Steady forced convection heat transfer from a heated circular cylinder to power-law fluids. Int. J. Heat Mass Tran 50 (5-6), 977-990.

10. Sivakumar P, Bharti RP and Chhabra RP (2007) Steady flow of power-law fluids across and unconfined elliptical cylinder. Chem. Eng. Sci., 62: 1682-1702.

11. Dhiman AK, Chhabra RP and Eswaran V (2006) Steady Flow of Power-law Fluids Across a Square Cylinder. Chem. Eng. Res. Des. 84:300-310.

12. Prhashanna A, Sahu AK and Chhabra RP (2011) Flow of power-law fluids past an equilateral triangular cylinder: Momentum and heat transfer characteristics. Int. J. Therm. Sci., 50: 2027-2041.

13. Neofytou P and Tsangaris S (2006) Flow effects of blood constitutive equations in 3D models of vascular anomalies. Int. J. Numer. Methods Fluids 51:489-510

14. Jung J, Lyczkowski RW, Panchal CB, Hassanein A (2006) Multiphase hemodynamic simulation of pulsatile flow in a coronary artery. J. Biomech. 39:2064-2073.

15. Hanafizadeh P, Mirkhani N, Davoudi MR, Masouminia M and Sadeghy K (2016) Non-Newtonian blood flow simulation of diastolic phase in bileaflet mechanical heart valve implanted in a realistic aortic root containing Coronary arteries. Artif. Organs 40:E179-E191.

16. Boyd J, Buick JM and Green S (2007) Analysis of the Casson and Carreau-Yasuda non-Newtonian blood models in steady and oscillatory flows using the lattice Boltzmann method. Physics of Fluids 19 (093103) 2007; https://doi.org/10.1063/1.2772250

17. Khechiba K, Mamou M, Hachemi M, Delenda N and Rebhi R (2017) Effect of Carreau-Yasuda rheological parameters on subcritical Lapwood convection in horizontal porous cavity saturated by shear-thinning fluid. Physics of Fluids 29, 063101 (2017); https://doi.org/10.1063/1.4986794

18. Kefayati GHR and Tang H (2018) MHD thermosolutal natural convection and entropy generation of Carreau fluid in a heated enclosure with two inner circular cold cylinders, using LBM. Int. J. Heat Mass Transfer. 126 (2018) 508–530.

19. Coelho PM and Pinho FT (2003) Vortex shedding in cylinder flow of shear-thinning fluids I. Identification and demarcation of flow regimes. J. Non-Newtonian Fluid. Mech., 110:143-176.

20. Coelho PM and Pinho FT (2003) Vortex shedding in cylinder flow of shear-thinning fluids II. Flow characteristics. J. Non-Newtonian Fluid. Mech., 110:177-193.

21. Coelho PM and Pinho FT (2003) Vortex shedding in cylinder flow of shear-thinning fluids III. Pressure measurements. J. Non-Newtonian Fluid. Mech., 121:55-68.

22. Haque S, Lashgari I, Giannetti F and Brandt L (2012) Stability of fluids with shear-dependent viscosity in the lid-driven cavity. J. Non-Newtonian Fluid. Mech., 173-174:49-61.

23. Lashgari I, Pralits JO, Giannetti F and Brandt L (2012) First instability of the flow of shear-thinning and shear-thickening fluids past a circular cylinder. J. Fluid. Mech., 701:201-227.

24. Pantokratoras A (2016) Steady flow of a non-Newtonian Carreau fluid across an unconfined circular cylinder. Meccanica, 51:1007-1016.

25. Mittal R, Dong H, Bozkurttas M, Najjar FM, Vargas A and von Loebbecke A (2008) A versatile sharp interface immersed boundary method for incompressible flows with complex boundaries. J. Comp. Phys., 227:4825-4852.

26. Kim J, Kim D and Choi H (2001) An immersed boundary finite volume method for simulations of flow in complex geometries. J. Comp. Phys., 207:457-492.

27. Liu C, Sheng X and Sung CH (1998) Preconditioned multigrid methods for unsteady incompressible flows. J. Comp. Phys., 139:35-57.

28. Roshko A (1953) On the development of turbulent wakes from vortex streets. NACA TN-2913.

29. Williamson CHK (1996) Vortex Dynamics in the Cylinder Wake. Annu. Rev. Fluid. Mech., 28:477-539.